

Static and Dynamic Characteristics of the Aerodynamic Forces on Pitching Airfoils between 0 to 360 degrees Angle of Attack

Moatasem Fouda*, Nabil M. khalifa[†], Mahmoud Rashad[‡], Mingdong Shao[§], Mostafa Elsharif[¶], and Haithem E. Taha [∥] *University of California, Irvine, CA, 92697, USA*

Pitching airfoils of sections NACA 0012, NACA 0015, and NACA 0021 performing a complete rotation with different pitching rates are tested to study their aerodynamic characteristics at Reynolds numbers: 60,000, 100,000, and 135,000. Each wing is mounted vertically inside the wind tunnel test section. A four-axis load cell is mounted underneath the test section to measure the lateral forces and the two in-plane horizontal moments. A stepper motor, driven by a micro-stepping driver, is used to accurately control the angle of attack (AOA). An incremental digital encoder is used to measure the real-time variation of the AOA. All real-time signals are sampled using the same data acquisition system. Results show that the maximum lift coefficient and the corresponding angle of attack depends on pitch rate, where a significant increase in their values is observed at high angular speeds.

I. Nomenclature

 α = Angle of attack AOA = Angle of attack AR = aspect ratio b = wingspan

c = chord

 C_L = Lift Coefficient

 $C_{L_{max}}$ = Maximum Lift Coefficient

 C_D = Lift Coefficient

 δ = Boundary Correction Factor

 ϵ_{tot} = Total Solid and Wake Blockage Correction Factor

Re = Reynolds Number $\sigma_{\overline{n}}$ = Standard error S = Wing Surface Area

 ω = wing model pitching velocity or stepper motor rotational speed

II. Introduction

Modeling aerodynamic characteristics for airfoils has been quite a need for the last decades, especially with the rise of renewable energy demand and the study of wind turbines. The operation of wind turbines [1, 2] is essentially an airfoil operating in a dynamic stall condition, where it could be a moderate or severe condition. Either way, models predicting different loads over the airfoil in dynamic stall such as the ONERA [3] and Beddoes–Leishman [4] requires the experimental lift and drag characteristics to be provided for the range of operation. However, some wind turbines could be operating in a significantly stalled region (angles of attack beyond 900 and 2000) where the aerodynamic characteristics should be established for model implementation. One of the pioneering studies was the study of the static lift curve from 00 to 1800 by Critzos et al. [5], but the dynamic stall models do not only require the static values but it is

^{*}PhD Student, Mechanical and Aerospace Engineering, 5200 Engineering Service Rd, Irvine, CA 92617, AIAA student member.

[†]PhD Student, Mechanical and Aerospace Engineering, 5200 Engineering Service Rd, Irvine, CA 92617, AIAA student member.

[‡]Visiting undergraduate Student from the German University at Cairo.

[§]Undergraduate Student, Mechanical and Aerospace Engineering Department, AIAA student member.

Visiting Undergraduate Student from the German University at Cairo.

Associate Professor, Mechanical and Aerospace Engineering, 5200 Engineering Service Rd, Irvine, CA 92617, AIAA Senior member.

also seeking to simulate a dynamic response of the airfoil, so it needs a dynamic response. One of the attempts to study this response was made by Jumper [6], but the maximum angle of attack in this study was limited to 450, where modern wind turbines go beyond this value. Another recent study by Truong [7] was done in an attempt to overcome this drawback by offering experimental results and dynamic response for airfoil performing a complete pitching cycle for 360°.

In this study, we are studying the aerodynamic response for a pitching airfoil with different angular speeds performing a complete rotation at Reynolds numbers of 60,000, 100,000, and 135,000 experimentally.

III. Experimental Setup

A. Wings

Three rectangular wings of chord 150mm and span of 300 mm were tested. These three wings are of the following sections:

- 1) NACA 0012
- 2) NACA 0015
- 3) NACA 0021

These wings are 3D printed of a PC-ABS plastic alloy, then post-processed and painted in black for future flow visualization. In addition to the steel rod, which attaches the wing model to the stepper motor, these wings are also reinforced by two carbon fiber rods in a symmetric way relative to the center of mass in order not to affect the center of mass position. Furthermore, all wings are equipped with removable upper and lower end plates to study the effect of the end plate on the span-wise flow.

B. Wind Tunnel and Test Section Calibration

The Wind Tunnel used in this experiment is a subsonic AEROLAB Eiffel Wind Tunnel (fig. 3)[8]. Test Section dimensions are 30"x30"x47". Maximum Speed is30 m/s with zero blockage in case of no model is mounted in the test section. The air velocity in the test section is measured by two static rings; the first ring is mounted downstream the contraction section inlet, while the second one is mounted upstream the test section.

The wind tunnel test section was calibrated using a pitot tube and digital manometer. The pitot tube was mounted on a mechanism designed to scan defined locations in a polar coordinates fashion. The air speed is measured at twelve points; Six points at radius 290mm and the other six points are 145mm. The gap between the the points at each radius is 60 degrees (Fig. 1). The airspeed values measured by the pitot tube are the same at all points of the whole permissible range of the wind tunnel fan rotational speed except for the lowest point near to the wind tunnel section floor. This slight decrease in the air speed at this point may be caused by the shear boundary layer near to the floor(Fig. 2-a). The airspeed values are consistent with the airspeed measured by the two static rings (Fig. 2-b). The airspeed values became scattered for the air speeds less than 5m/s. This slight dispersion agrees with AEROLAB guidelines regarding the airspeed instability for values less than 5 m/s.

This average airspeed measured by the two static rings is affected by the blockage caused by the wing model, especially at $\alpha=90^\circ$. The wind tunnel is controlled by a manufacturer-made LabVIEW program equipped with a PID controller. The PID controller could be fed by either the rpm or the airspeed as measured by the two static rings. If the PID controller is set to maintain the wind tunnel speed, it will increase the speed to keep the average speed measured by the two static rings and accommodate for the blockage. This compensation looks good for maintaining the average speed, but it will increase the wing model's local speed. So we used the fan rpm as the feedback parameter, not the average speed to be controlled by the PID controller.

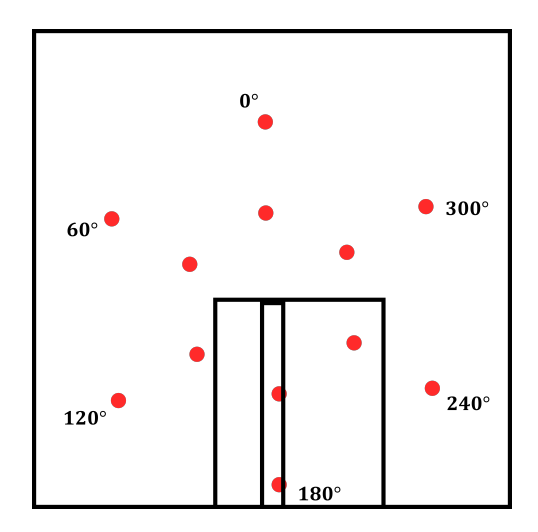


Fig. 1 Wind tunnel test section calibration points.

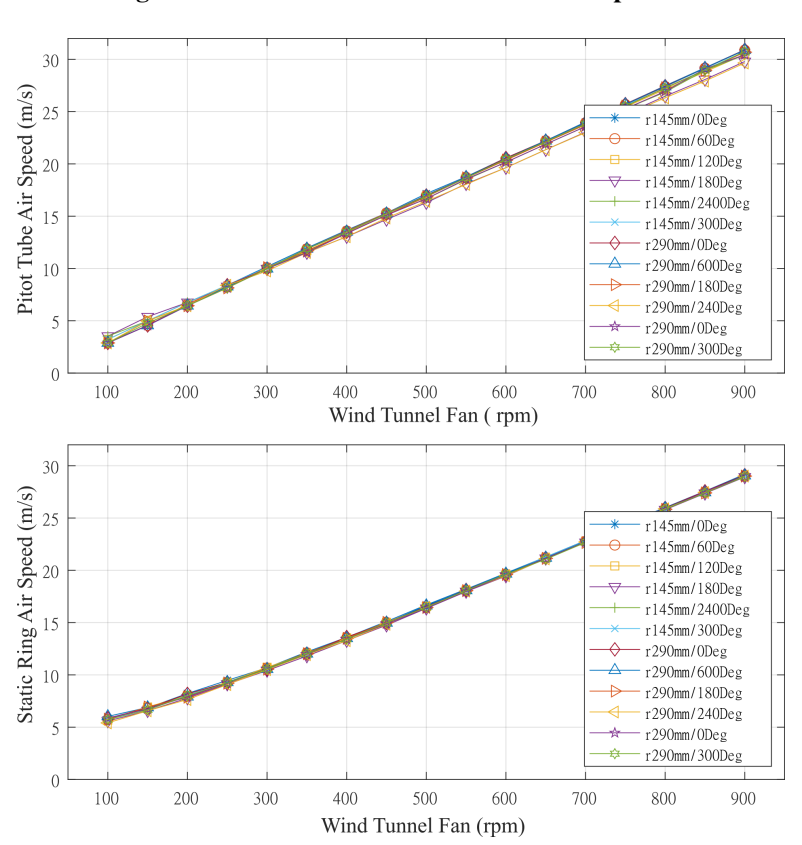


Fig. 2 Wind tunnel test section calibration results.

C. Wind tunnel vertical testing configuration

The wing model is mounted vertically using a steel rod reinforcing the rectangular wing model at its center of mass position to reduce the lateral inertial loads associated with the high speed or accelerating rotational motion. Each wing's center of mass is calculated numerically. These centers of masses were found to be as follows:

- 1) NACA 0012:41.97% of the chord
- 2) NACA 0015:41.63% for the chord

3) NACA 0021:41.73% for the chord

The metallic rod penetrates the floor of the wind tunnel test section through a hole with a sufficient gap to avoid any reaction forces emerging from the contact with the wind tunnel body under the highest aerodynamic force. The metallic rod is rigidly coupled with the shaft of a high torque NEMA 23 stepper. This stepper motor is mounted on the top of a Fouraxis load cell to measure the lateral Lift force, the vertical spanwise force, the two horizontal moments Mx and My (fig. 3).

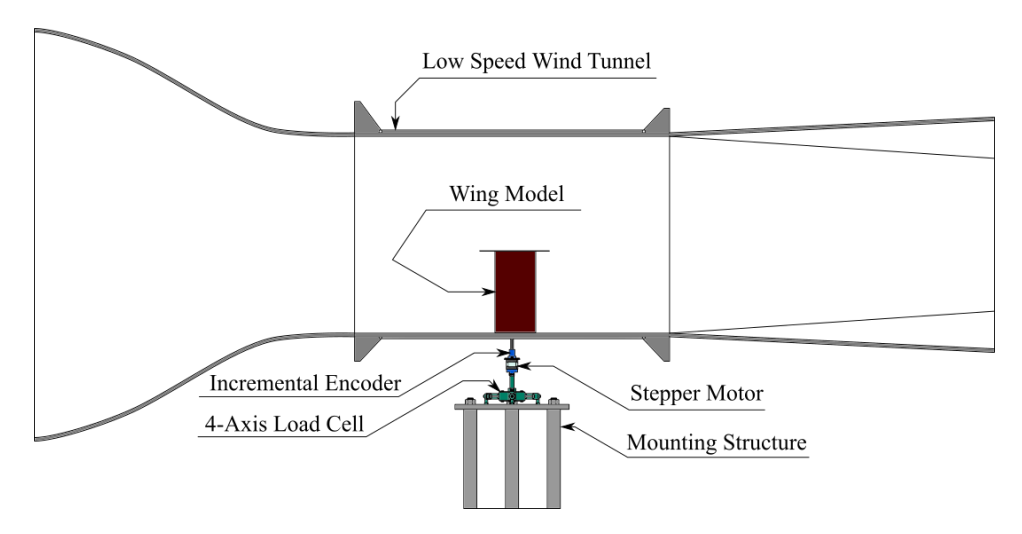


Fig. 3 Wind tunnel vertical testing configuration.

IV. Data Collection

A. Inertial loads filtration and data acquisition

In the first trials of this experiment, we found that the structural response of the experimental setup adds inertial loads to the aerodynamic loads, especially at angular speeds $\omega > 10 Deg/sec$. An anti-aliasing Butterworth analog low pass filter should be used before the sampling to exclude these high-frequency inertial loads from the low-frequency aerodynamic loads. Its cutoff frequency should be low enough to filter the natural frequency of the first mode. Impact hammer modal testing is used to measure the primary the natural frequency of the wing-stepper motor-load balance system. The natural frequency of the NACA0012 was found at 11 Hz, while the natural frequency of the heaviest wing model, NACA0021, was found at 10 Hz (fig. 4). The four low pass filters used in this experiment to filter the four signals of the load cell are of model USBPGF-S1 [9]. The maximum cutoff frequency to filter the primary structural response was found experimentally to be at 5Hz (fig. 5). The filtered signals are sampled at a rate of 200 Hz by the NI USB-6211 [10]. The load balance was designed and built specifically of the high AOAs wind tunnel experiments [11, 12, 12–16]. The bandwidth of this load cell was found experimentally to be at 60 Hz. The sensitivity of the load balance is 2mV/V, and the resolution is 0.04 N. The load balance is powered by an AC Wheatstone bridge excitation power supply PSM-R[17].

The step of the NEMA23 stepper motor is 0.9 Deg [18]. The stepper motor is driven by a DM542 digital micro-stepping stepper motor driver at 32,000 micro-stepping, making the final step 0.0056 degrees. The stepper motor was sized to provide a maximum torque higher than the required torque at the acceleration and deceleration of the heaviest wing, NACA 0021, at the highest Reynolds number. Although a motor with high output torque will not skip steps during the harshest rotation, the AOA is measured using another independent digital incremental encoder of type CUI AMT10 of resolution 2048 [19]. The digital encoder is mounted on the stepper motor and measures the motor shaft's angular position, while its digital signal is fed into the same DAQ used to sample the load cell signals. Because the analog signals of the load cell are filtered at a cutoff frequency of 5 Hz, while the digital signal of the encoder is not, there is a delay of about 0.12 seconds in the load cell readings from the encoder readings. This delay will be found in all figures presented in this paper, and it is more evident in the high angular speed graphs. It is also found that the response

of the aerodynamic forces becomes immediate if the LPF cutoff frequency becomes higher than 200 Hz.

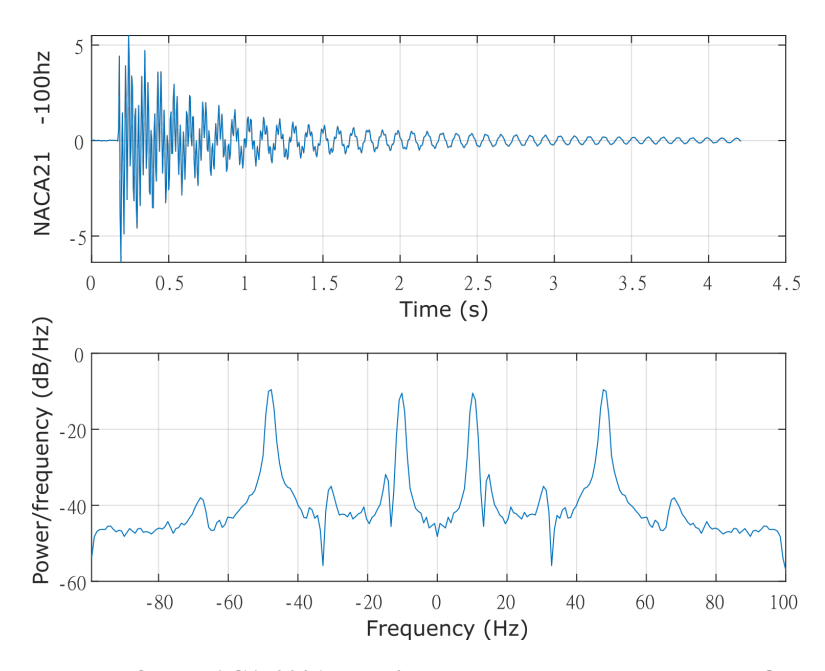


Fig. 4 The response of the NACA 0021 experimental setup to a hammer test-filtered at 100Hz.

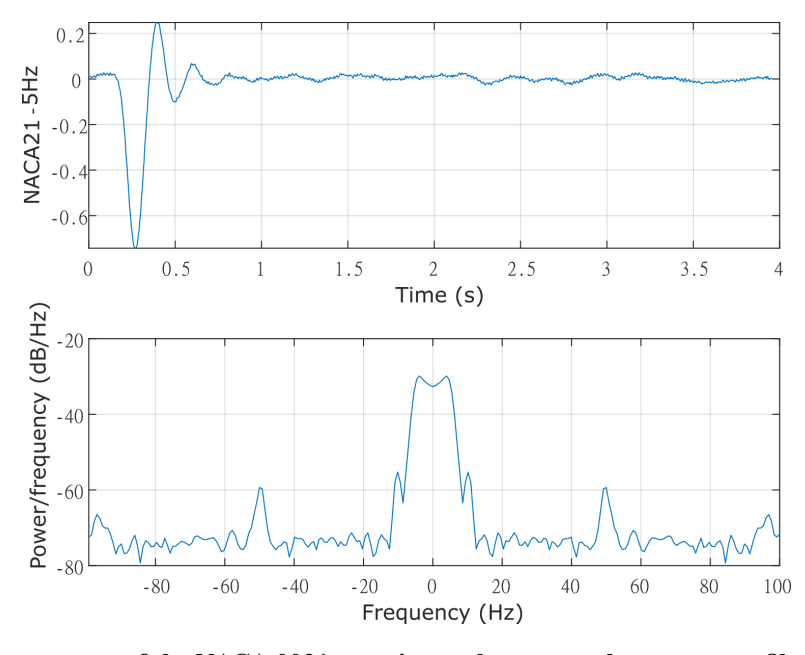


Fig. 5 The response of the NACA 0021 experimental setup to a hammer test-filtered at 5Hz.

The motion of the stepper motor is controlled by two Arduino codes designed for two modes of testing:

- 1) Static complete rotation testing; the code controls the motor motion to rotate 360 deg incrementally with adjustable parameters. For this experiment, the parameters are selected such that the wing rotates at a step of 1.8 deg, its incremental motion is at 30 deg/sec, and the wing stays at each step for 5 seconds for eliminating any steadiness in the flow due to the motion of the wing. At the last second of the five seconds, the aerodynamic forces are averaged for calculating the aerodynamic forces at this angular position.
- 2) Constant angular velocity complete rotation testing; the code controls the motor motion to rotate 360 deg

continuously for five times with adjustable parameters. For this experiment, the parameters are selected such that the wing rotates 360 degrees at angular velocities 5, 10, 20, 30, 45, 60, 90, 120, 180, 360 degrees per second, while the wing stays still between the five rotations for the larger of the 10 seconds or the half of the periodic time of the rational motion.

B. Data processing and frequency analysis

A data flow program was built using LabVIEW to process the load balance signals and the incremental encoder's digital signal. This LabVIEW program automatically exports real-time array for the four global forces; F_y , F_z , M_x and M_y of each experiment run separately. A Matlab code then handles these arrays for generating the required figures and analyzing the signals using the Fast Fourier and the CZT transforms to identify the lift coefficient's frequency and the frequencies of the shed vortices as measured by the load balance. Moreover, the LabView data flow program monitors, saves, and alarms for any overloading that may occur saves the maximum loading values reached during the experiments. It also performs a dynamic and static calibration for the load balance [11]. Fig. 6 shows a wiring diagram for the load balance connections with the power supply, LPFs, DAQ, and the interface program.

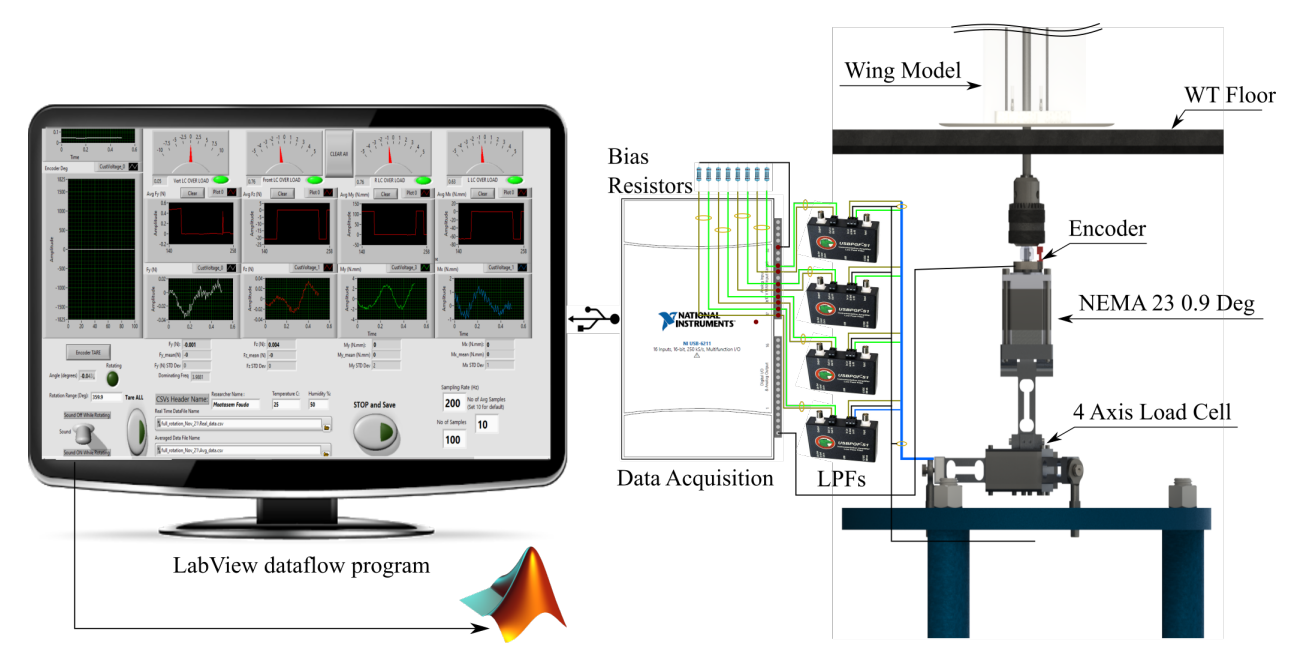


Fig. 6 Wiring diagram for the load balance.

C. Experimental Procedure and Data Processing

The experiment starts with taring the load balance from the LabView data-flow program, and then running the wind tunnel to the desired speed. Once the airspeed in the test section becomes steady, the stepper motor is given a signal according to the type and the speed of the run. When the experiment is finished, two CVS files are exported by the LabView for the real time and averaged data of the forces and the AOA and

V. Results and Discussion

Figures 7, 8, and 9 show the time-variation of the lift coefficient at different angular speeds, Reynolds numbers and airfoil sections. The figures clearly show that the maximum lift coefficient $C_{L_{max}}$ increases with the increase in the pitching angular velocity ω . This increase in the $C_{L_{max}}$ is a delay in the stall. This delay in stall may be explained in simple terms as follows. In order for the fluid particles to avoid separation from the upper surface of the wing at high angles of attack, they need more adhesion to the wing surface to sustain a sufficient centripetal force necessary for the largely curved path [20, 21]. The effect of pitching angular velocity ω on this process is reducing the relative speed

between the moving fluid particles and the leading edge (because the translational velocity of the leading edge due to pitching up is in the same direction as the flow). Since the relative velocity between the fluid particles and wing upper surface at the leading edge is reduced, less centripetal force will be required, and the separation will be delayed [21]. On the other hand, since pitching is performed around 42% of the chord, the relative velocity is increased on most of the lower surface (58% of the chord), resulting in higher dynamic pressure. Both of these two effects lead to an increase in $C_{L_{max}}$.

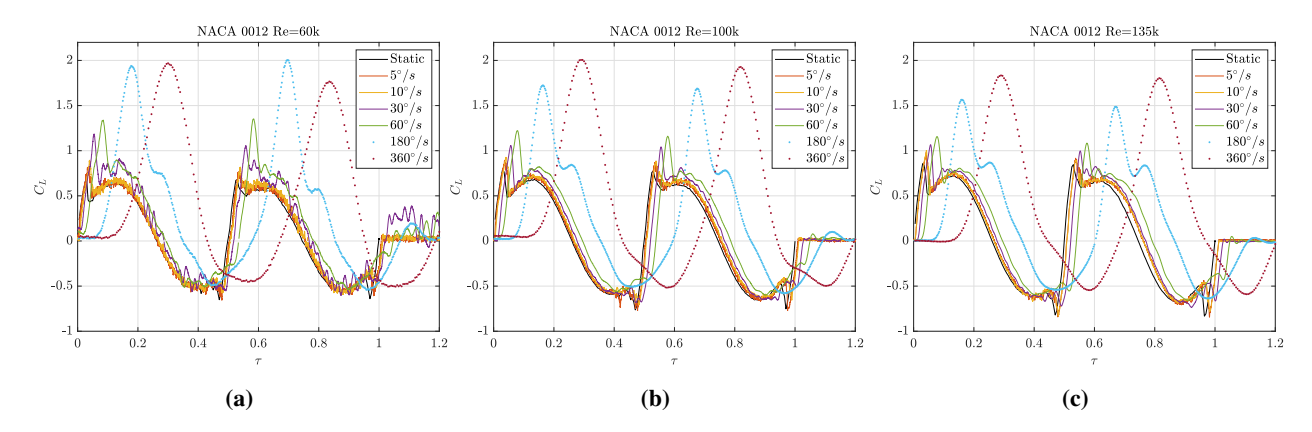


Fig. 7 Rotating NACA0012 Wing at three different Reynolds numbers:(a) Re=60k, (b) Re=60k, and (c) Re 135k.

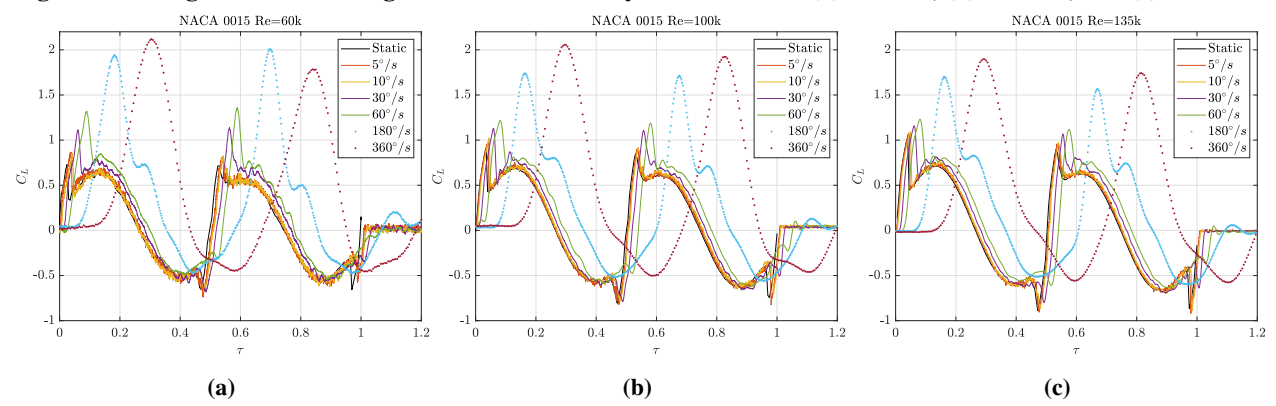


Fig. 8 Rotating NACA0015 Wing at three different Reynolds numbers:(a) Re=60k, (b) Re=60k, and (c) Re 135k.

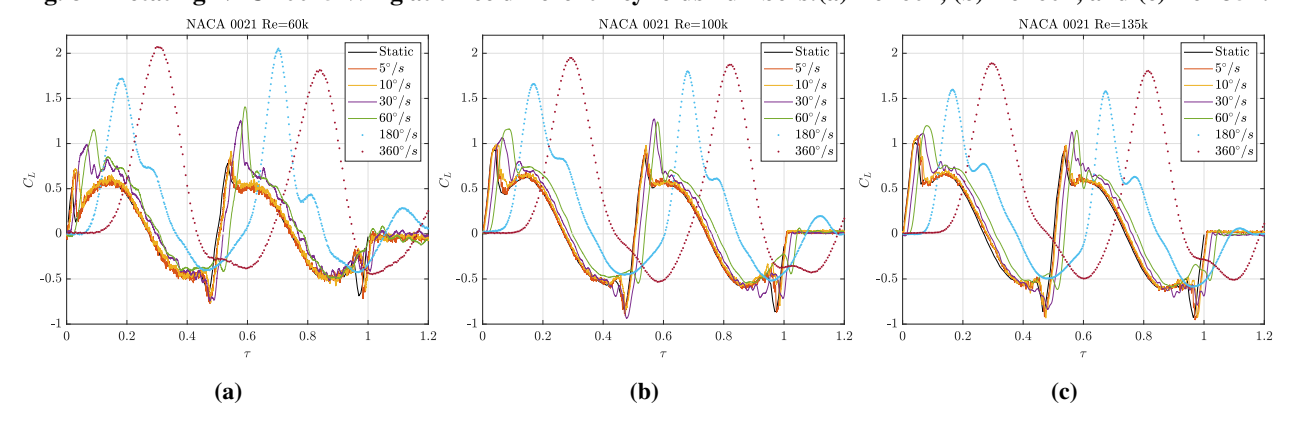


Fig. 9 Rotating NACA0021 Wing at three different Reynolds numbers:(a) Re=60k, (b) Re=60k, and (c) Re 135k.

Figures 11, 12, and 13 provide the same data of Figs. 7, 8, and 9 in a different format to accentuate the effect of Reynolds number. The figures show that the effect of Reynolds number in this range (Re = 60k - 135k) is not significant at low angular speeds; its effect increases with ω . The effect of Reynolds number is found to play an opposite role to the pitching velocity's. Since the viscosity does not change, the increase in the Reynolds number is just an increase in the fluid velocity. As discussed above, the larger the velocity, the larger the centripetal force required to maintain the largely curved path of the fluid particles (i.e., to keep the fluid particles attached to the wing's upper surface near the leading edge). This effect will promote separation in the immediate vicinity of the leading edge, which decreases $C_{L_{max}}$ (see Fig. 14).

If the same analogy is used to study the effect of the wing cross-section on dynamic stall, the leading edge radius should be the main focus. The leading edge radius of each airfoil was measured as a percentage of the chord follows:

- 1) NACA 0012:Leading edge radius equals 1.8% of the chord
- 2) NACA 0015:Leading edge radius equals 2.4% of the chord
- 3) NACA 0021:Leading edge radius equals 5.1% of the chord

The centripetal force required to maintain a particle moving with a certain velocity on a curvilinear path is directly proportional to curvature of the path (i.e., inversely proportional to the radius). So, the decreased leading edge radius (from NACA 0021 to NACA 0012) should expedite the stall similar to the effect of Reynolds number, but the leading edge separation is not only dictated by the surface curvature, but also how long the particle maximum lift coefficient of the pitching inverted airfoil (i.e., the moves on that curved path. In all wings, the stagnation point remains at the same angular displacement from the leading edge point since the angle of attack is the same. Despite this identical angular displacement, in the thicker airfoils, the fluid particle cut a longer distance s_p from the stagnation point to the end of the leading edge circular curvature (see Fig. 10); and the longer the distance along a curved path, the more susceptibility to separation. In conclusion, these two effects seem to act against each other and may reduce the effect of the airfoil section on dynamic stall (see Figs. 7 and 11).

The last paragraph is in line with the results of $C_{L_{max}}$ over an inverted airfoil, as demonstrated in the second peak in the lift coefficient graphs (Figs. 7, 8, and 9). In most cases, the maximum lift coefficient of the pitching inverted airfoil (i.e., the second peak) is larger than that of the normal airfoil. This can be explained in simple terms as follows. The relative velocity between the leading point (trailing edge in the inverted case) and the surrounding flow becomes slightly larger in the inverted airfoil case because of the increased rotation radius (58% versus 42%). For example, at Re=100k, the relative velocity at the leading edge equals 9.34m/s, while it is 9.19m/s at the trailing edge when the airfoil is inverted. So perhaps the major difference between the pitching wing in the conventional configuration and the inverted configuration is the curvature of the path near the leading point. While the sharpness of the trailing edge (the leading point in the inverted case) may be expected to promote separation, the forwardly inclined surface of the airfoil near the leading point (i.e., trailing edge) seem to guide the airflow along the curved path, mitigating the sharpness effect of the leading point, perhaps in the expense of additional drag. As a result, the maximum lift coefficient $C_{L_{max}}$ of the inverted airfoil (the second peak) is slightly higher than $C_{L_{max}}$ of the normal airfoil (the first peak), particularly for NACA 0021, as shown in Figs. 7, 8, and 9.

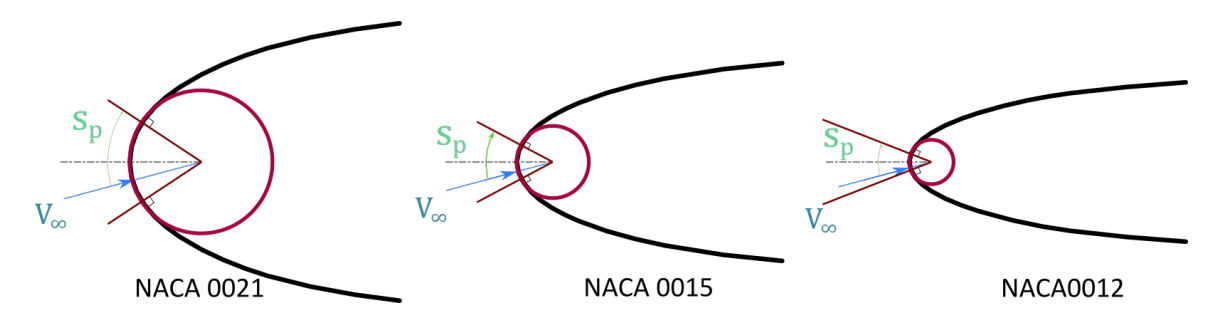


Fig. 10 Magnified schematic for the distance s_p cut by a fluid particle over the leading edge circular surface for NACA0021, 0015, and 0012 at the same AOA.

The interpretations of these experimental results found in this section could be supported by more experimental tests using the same airfoils at the same different pitching rate but changing the location of the center of rotation to different

locations on the chord, including the leading edge position itself. This parameter will enable studying the leading edge relative velocity effect at the same pitching rate. Also, it requires testing symmetric sections like a flat plate and ellipse of different aspect ratios.

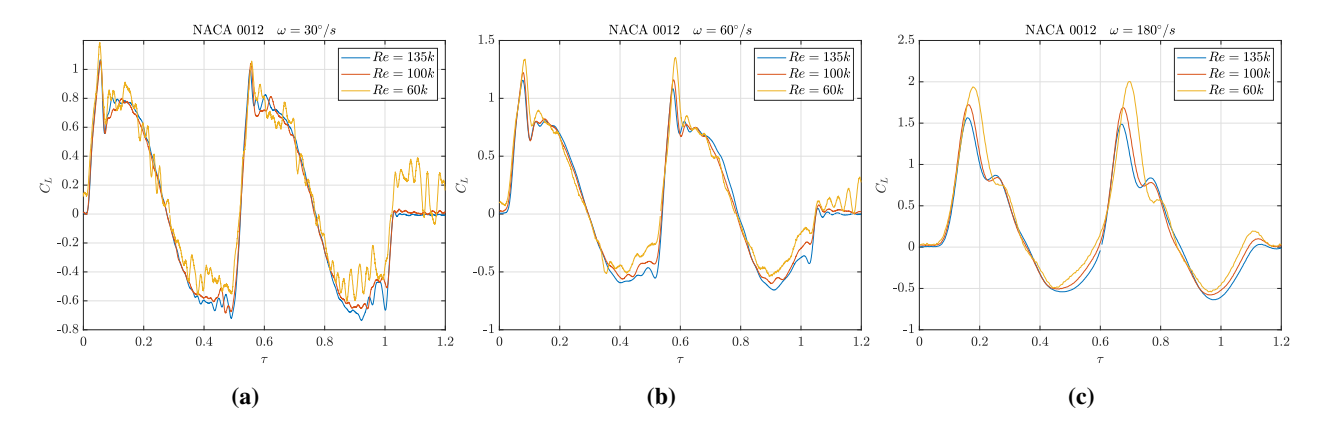


Fig. 11 Rotating NACA0012 Wing at three different angular velocities:(a) $\omega = 30^{\circ}/s$, (b) $\omega = 60^{\circ}/s$, and (c) $\omega = 180^{\circ}/s$.

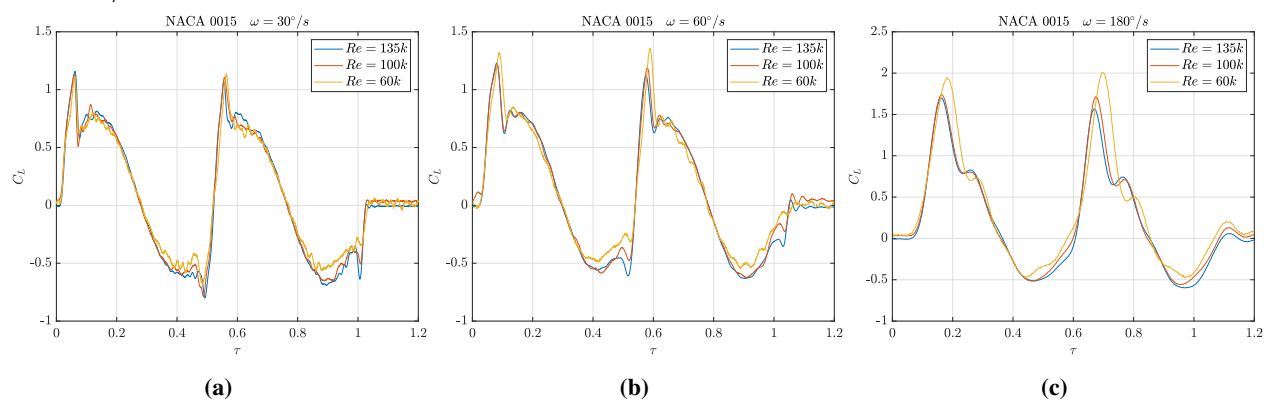


Fig. 12 Rotating NACA0015 Wing at three different angular velocities:(a) $\omega = 30^{\circ}/s$, (b) $\omega = 60^{\circ}/s$, and (c) $\omega = 180^{\circ}/s$.

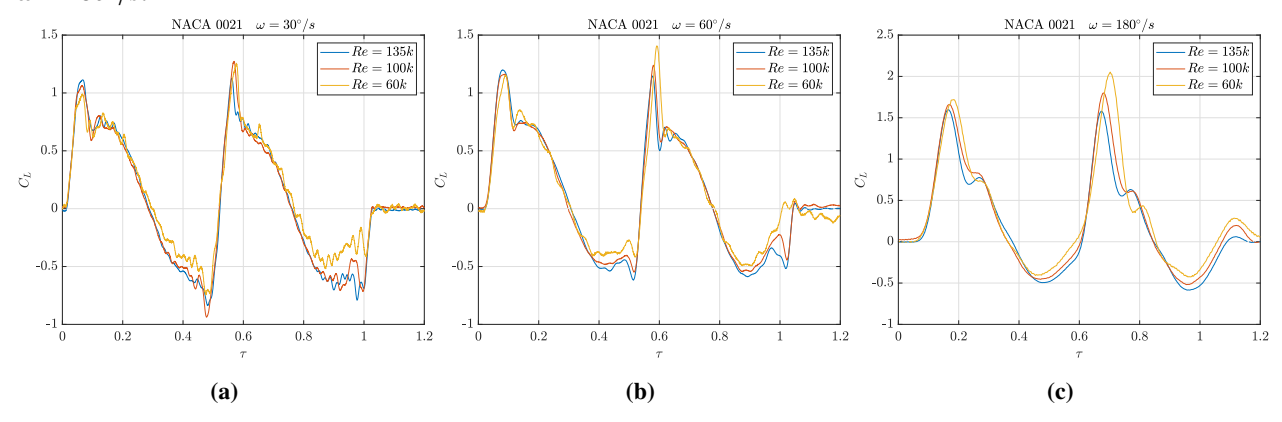


Fig. 13 Rotating NACA0021 Wing at three different angular velocities:(a) $\omega = 30^{\circ}/s$, (b) $\omega = 60^{\circ}/s$, and (c) $\omega = 180^{\circ}/s$.

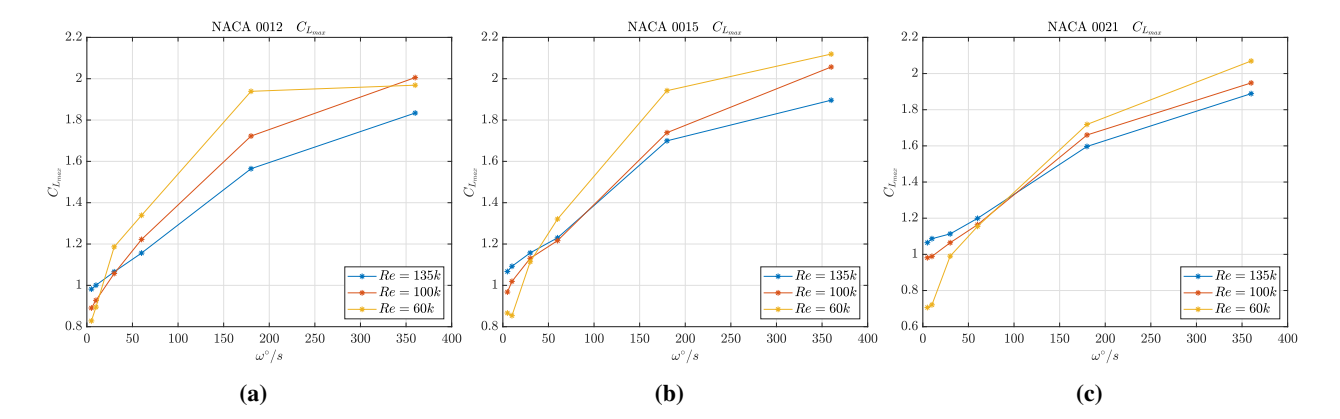


Fig. 14 Maximum lift coefficient versus the angular speed at different Reynolds numbers for the three studied airfoils.

VI. Conclusion

Both pitching angular velocity and Reynolds number affect the maximum lift coefficient $C_{L_{max}}$ during dynamic stall. A larger pitching rate increases $C_{L_{max}}$, while a larger Reynolds number decreases it. These behaviors can be well explained if we postulate that the flow can sustain up to a certain maximum limit of curvature (centripetal force). In this case, the effect of increasing the Reynolds number (i.e., increasing velocity) is demanding more centripetal force, promoting separation. On the other hand, the larger the pitching angular velocity, the larger the translational speed of the leading edge (which is in the same direction of the oncoming flow during pitching up); the smaller the relative velocity of the leading edge with respect to the surrounding flow, which demands less centripetal force, hence delaying separation and increasing $C_{L_{max}}$. The thickness of the wing cross-section and the radius of the leading edge seem to have less effects on $C_{L_{max}}$.

Acknowledgments

This material is based upon work supported by the Air Force Office of Scientific Research under award number FA9550-19-1-0126, monitored by Dr G. Abate. The first author would like to acknowledge the efforts of Jay Nilesh Ahir (UCI) in modelling the wing models and preparing its surfaces for the wind tunnel experiments.

References

- [1] Vries, O. D., "On the theory of the horizontal-axis wind turbine," *Annual review of fluid mechanics*, Vol. 15, No. 1, 1983, pp. 77–96.
- [2] Bhutta, M. M. A., Hayat, N., Farooq, A. U., Ali, Z., Jamil, S. R., and Hussain, Z., "Vertical axis wind turbine–A review of various configurations and design techniques," *Renewable and Sustainable Energy Reviews*, Vol. 16, No. 4, 2012, pp. 1926–1939.
- [3] Petot, D., "Progress in the semi-empirical prediction of the aerodynamic forces," 1983.
- [4] Leishman, J. G., and Beddoes, T., "A Semi-Empirical model for dynamic stall," *Journal of the American Helicopter society*, Vol. 34, No. 3, 1989, pp. 3–17.
- [5] Critzos, C. C., Heyson, H. H., and Boswinkle Jr, R. W., "Aerodynamic characteristics of NACA 0012 airfoil section at angles of attack from 0 deg to 180 deg," Tech. rep., NATIONAL AERONAUTICS AND SPACE ADMINISTRATION WASHINGTON DC, 1955.
- [6] Jumper, E., Schreck, S., and Dimmick, R., "Lift-curve characteristics for an airfoil pitching at constant rate," *Journal of aircraft*, Vol. 24, No. 10, 1987, pp. 680–687.

- [7] Truong, V., "An analytical model for airfoil aerodynamic characteristics over the entire 360° angle of attack range," *Journal of Renewable and Sustainable Energy*, Vol. 12, No. 3, 2020, p. 033303.
- [8] AeroLab Subsonic Wind Tunnel 30, AEROLAB, ????
- [9] USB Programmable Single Channel Instrumentation Amplifier and Low-Pass Filter data sheet, Alligator Technologies, ???? URL https://alligatortech.com/downloads/USBPGF-S1_Data_Sheet.pdf.
- [10] NI USB-621x User Manual, National Instruments, ???? URL https://www.ni.com/pdf/manuals/371931f.pdf.
- [11] Fouda, M., Shorbagy, M. A., and Taha, H. E., "Multi-axis Load Cell Provisional Patent,", 3 2021.
- [12] Fouda, M., and Taha, H. E., "Experimental Investigations of Airplane Maneuverability and Stability in Stall," *AIAA Scitech* 2021 Forum, 2021, p. 1819.
- [13] Fouda, M., and Taha, H. E., "Effect of Wing Planform on Airplane Stability and Control Authority in Stall," *AIAA Scitech* 2022 Forum, 2022.
- [14] Fouda, M., khalifa, N. M., Rashad, M., Shao, M., Elsharif, M., and Taha, H. E., "Effect of Mean Angle of Attack on Lift Dynamics over a Harmonically Pitching Airfoil," *AIAA Scitech 2022 Forum*, 2022.
- [15] Zakaria, M., Fouda, M., and Taha, H. E., "Experimental investigation of aerodynamic characteristics of a 4-winged flapping," AIAA Scitech 2022 Forum, 2022.
- [16] Shorbagy, M. A., El-hadidi, B., El-Bayoumi, G., Said, O., and Fouda, M., "Experimental Study on Bio-Inspired Wings with Tubercles," AIAA SciTech 2019 Forum, 2019, p. 0848.
- [17] Load cell power supply module adjustable from 4 to 15 VDC PSM-R data sheet, Transducer Techniques, ???? URL https://www.transducertechniques.com/pdf/psmr.pdf.
- [18] Nema 23 Bipolar 0.9deg 1.26Nm Stepper Motor Data Sheet, OMC-Stepperonline, ???? URL https://www.omc-stepperonline.com/download/23HM22-2804S.pdf.
- [19] AMT10 Modular Incremental Encoder Data Sheet, CUI Devices, ???? URL https://www.cuidevices.com/product/resource/amt10.pdf.
- [20] Gonzalez, C., and Taha, H., "An empirical extension to free-streamline methods: Modeling leading-edge separation," *Bulletin of the American Physical Society*, 2021.
- [21] Taha, H., and Gonzalez, C., "A Variational Theory of Lift," Bulletin of the American Physical Society, 2021.